

Polarization microscopy by use of digital holography: application to optical-fiber birefringence measurements

Tristan Colomb, Florian Dürr, Etienne Cuche, Pierre Marquet, Hans G. Limberger, René-Paul Salathé, and Christian Depeursinge

We present a digital holographic microscope that permits one to image polarization state. This technique results from the coupling of digital holographic microscopy and polarization digital holography. The interference between two orthogonally polarized reference waves and the wave transmitted by a microscopic sample, magnified by a microscope objective, is recorded on a CCD camera. The off-axis geometry permits one to reconstruct separately from this single hologram two wavefronts that are used to image the object-wave Jones vector. We applied this technique to image the birefringence of a bent fiber. To evaluate the precision of the phase-difference measurement, the birefringence induced by internal stress in an optical fiber is measured and compared to the birefringence profile captured by a standard method, which had been developed to obtain high-resolution birefringence profiles of optical fibers. © 2005 Optical Society of America

OCIS codes: 090.1760, 110.0180, 110.2350, 260.1440, 260.5430.

1. Introduction

Digital holography takes advantage of the performance of the classical holographic technique but adds the advantages of the digital approach. Indeed, classical holography was the first imaging technique that permitted one to record simultaneously the amplitude and the phase components of a wavefront, but it had a major disadvantage: less quantitative results, lower access rate, and less flexibility in data processing. The development of sensitive and fast acquisition devices, such as charge-coupled devices (CCD) sensors, and the computational power increase of personal computers allowed the birth of digital holography and therefore a fast accessibility to quantitative results. Even if classical holography evolved to allow quick image reconstruction (a minute or less),¹ it is still far from the performances of certain types of digital cameras used, for example, by Pedrini

et al. in Ref. 2 (600 frames/s) and far from reconstruction rate (less than 1 Hz in Ref. 3 and about 10 reconstructions per second).

Introducing a microscope objective (MO) to increase the spatial resolution was done in holography a long time ago,⁴ is now a basic procedure in digital holography,^{3,5-7} and allows amplitude and phase contrast imaging with a spatial resolution of better than 1 μm in all dimensions.³

Another procedure already proposed in classical holography is to record on the same support different interference patterns (multiexposed holograms). A first possibility is to record these interferences by changing the reference-wave orientation. As a consequence, when the hologram is illuminated, different reconstructed objects appear, depending on the orientation of the illumination wave. Well known examples are the artistic holograms where we can observe a human face that is smiling or not when looking at it from the left or from the right. Another possibility is to record simultaneously the interference between an object wave and several reference waves as suggested by Lohmann in 1965,⁸ and especially using two different polarizing reference waves. If the first possibility has no real interest in digital holography, the second one can be applied easily as presented in Refs. 9 and 10 and allows polarization imaging by use of a single hologram.

Other techniques allow state-of-polarization (SOP) imaging, but most of them need polarizing-analyzing

T. Colomb (tristan.colomb@epfl.ch), F. Dürr, H. G. Limberger, R.-P. Salathé, and C. Depeursinge are with Imaging and Applied Optics Institute, Ecole Polytechnique Fédérale de Lausanne (EPFL), CH-1015 Lausanne, Switzerland. E. Cuche is with Lyncée Tec SA, rue du Bugnon 7, CH-1005 Lausanne, Switzerland. P. Marquet is with the Department of Physiology, University of Lausanne, CH-1005 Lausanne, Switzerland.

Received 7 June 2004; revised manuscript received 6 December 2004; accepted 17 March 2005.

0003-6935/05/214461-09\$15.00/0

© 2005 Optical Society of America

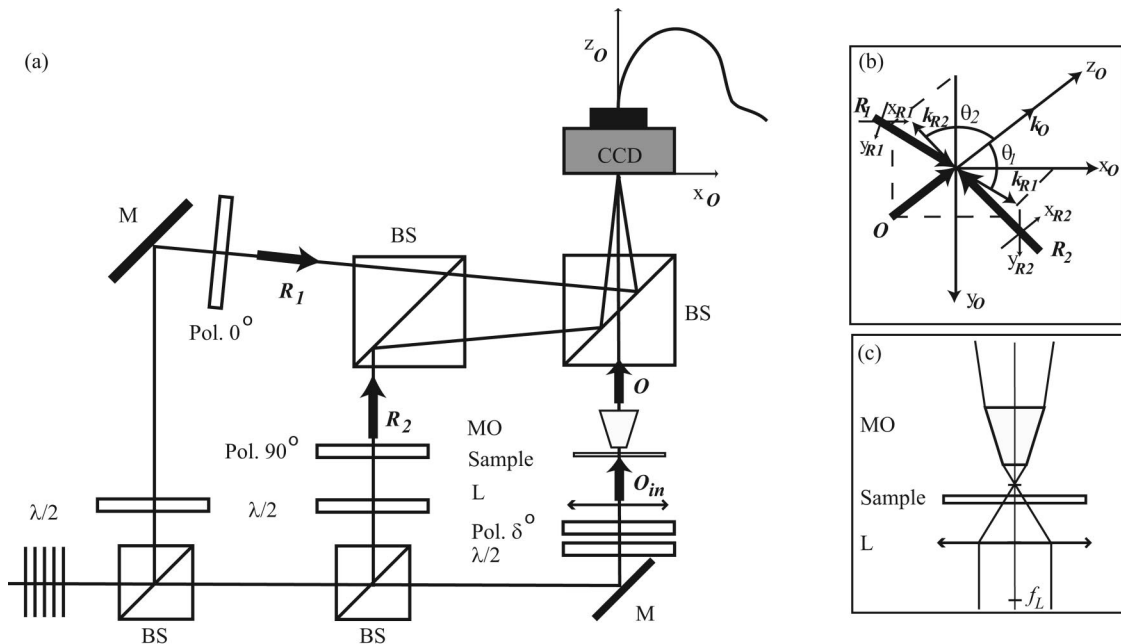


Fig. 1. (a) Experimental setup. \mathbf{O}_{in} illuminating wave, \mathbf{O} object wave; \mathbf{R}_1 and \mathbf{R}_2 , polarized reference waves; Pol. α° , polarizer oriented at α° ; $\lambda/2$, half-wave plate; M, mirror; BS, beam splitter; L, lens with focal length f_L ; MO, the microscope objective, and CCD, the change-coupled device. (b) Detail showing the off-axis geometry at the incidence on the CCD. The $x_O y_O$ plane is parallel to the CCD camera. \mathbf{R}_1 in the $y_O z_O$ plane and \mathbf{R}_2 in the $x_O z_O$ plane are coming from different spatial directions. (c) Detail showing the ray tracing in the object arm. The collimated beam focalized with the lens L illuminates a small portion of the sample placed between the lens L and its focal plane. The MO magnifies the transmitted beam to produce a divergent beam that covers the entire chip area of the CCD.

optics (polarizers, rotators, and retarders) that must be adjusted at various settings, requiring a long setting time compared to the acquisition performances of a CCD. The temporal resolution can be improved by use of a liquid-crystal universal compensator in place of analyzing optics,¹¹ but the technique still needs several images to reconstruct SOP. Finally other methods very similar to holographic ones allow SOP imaging with a single acquisition,^{12,13} but their main drawback is a relatively low spatial resolution compared to polarizing-analyzing techniques that can use a microscope objective to improve the spatial resolution.

Here, by the introduction of a MO in the setup, the polarization digital holography (Pol-DH) method evolves to polarization digital holographic microscopy (Pol-DHM) by combining the method of Refs. 3 and 9. To illustrate the method, a bent optical fiber is used to study the induced birefringence. To evaluate the precision of the method, the birefringence due to fiber internal stresses is measured by Pol-DHM with two different MOs and compared with the birefringence profile captured with a high-resolution standard method.

2. Method

A. Polarization Microscope Design

The Pol-DHM geometry presented in Fig. 1(a) is designed for transmission imaging with transparent samples. The basic architecture is that of a Mach-Zehnder interferometer with two orthogonally lin-

early polarized reference waves that interfere with an object wave in off-axis geometry as presented in Fig. 1(b).

The incident-object plane wave \mathbf{O}_{in} is focalized by a lens L (focal $f_L = 30$ mm, $NA \cong 0.07$) to illuminate a small portion of the sample with a known linear polarization state determined by the orientation of a polarizer [Pol. δ° in Fig. 1(a), $\delta = 45^\circ$ for the applications presented here]. The position of the sample is adjusted to produce a magnified image of the sample with the MO at a distance d behind the CCD ($d \cong 5$ cm). The transmitted light collected by the MO produces a wavefront called object wave \mathbf{O} . The SOP of the object wave is different from the illuminating wave \mathbf{O}_{in} and results from the sample birefringence properties integrated along the propagation direction. Then the wave \mathbf{O} diverges from the MO to cover the entire chip of the CCD placed at 15 cm from the MO. To simplify the theoretical analysis of polarization, we define a single propagation vector \mathbf{k}_O perpendicular to the CCD plane ($x_O y_O$).

The reference waves \mathbf{R}_1 and \mathbf{R}_2 , respectively polarized horizontally (along x_{R1}) and vertically (along y_{R2}) by polarizers [Pol. in Fig. 1(a)], reach the CCD camera with a small incidence angle θ_1 and θ_2 , respectively ($\theta_1 \cong 2.5^\circ$, $\theta_2 \cong 3^\circ$). To avoid any interference between the reference waves, the vectors x_{R1} and y_{R2} should be orthogonal; therefore, the directions of propagation \mathbf{k}_{R1} and \mathbf{k}_{R2} should be respectively in the planes $y_O z_O$ and $x_O z_O$.

Using the Jones formalism, the different waves are written

$$\begin{aligned}
\mathbf{O} &= \begin{pmatrix} |o_1| \exp(\phi_o) \\ |o_2| \exp(\phi_o + \Delta\phi_o) \\ 0 \end{pmatrix} \exp[i(\mathbf{k}_o \cdot \mathbf{r})] \\
&= \begin{pmatrix} o_1 \\ o_2 \\ 0 \end{pmatrix} \exp[i(\mathbf{k}_o \cdot \mathbf{r} + \phi_o)], \\
\mathbf{R}_1 &= \begin{pmatrix} r_1 \\ 0 \\ 0 \end{pmatrix} \exp[i\mathbf{k}_1 \cdot \mathbf{r}], \\
\mathbf{R}_2 &= \begin{pmatrix} 0 \\ r_2 \\ 0 \end{pmatrix} \exp[i\mathbf{k}_2 \cdot \mathbf{r}], \tag{1}
\end{aligned}$$

where $\mathbf{r} = (x, y, z)$ is the position vector, $\phi_o = \phi_o(x, y)$ is the sample optical phase delay seen by a linear horizontal polarized wave, and $\Delta\phi_o$ is the phase difference. The wave vectors are written

$$\begin{aligned}
\mathbf{k}_o &= \frac{2\pi}{\lambda} \begin{bmatrix} 0 \\ 0 \\ 1 \end{bmatrix}, \quad \mathbf{k}_1 = \frac{2\pi}{\lambda} \begin{bmatrix} 0 \\ \sin(\theta_1) \\ \cos(\theta_1) \end{bmatrix}, \\
\mathbf{k}_2 &= \frac{2\pi}{\lambda} \begin{bmatrix} -\sin(\theta_2) \\ 0 \\ \cos(\theta_2) \end{bmatrix}, \tag{2}
\end{aligned}$$

where λ is the wavelength of the laser used, in our case a He-Ne laser emitting at 633 nm.

At the output of the interferometer the interference between \mathbf{O} , \mathbf{R}_1 , and \mathbf{R}_2 creates the hologram intensity distribution

$$\begin{aligned}
I_H(x, y) &= (\mathbf{R}_1 + \mathbf{R}_2 + \mathbf{O}) \cdot (\mathbf{R}_1 + \mathbf{R}_2 + \mathbf{O})^* \\
&= |\mathbf{R}_1|^2 + |\mathbf{R}_2|^2 + |\mathbf{O}|^2 + \mathbf{R}_1 \mathbf{O}^* + \mathbf{R}_2 \mathbf{O}^* \\
&\quad + \mathbf{R}_1^* \mathbf{O} + \mathbf{R}_2^* \mathbf{O}. \tag{3}
\end{aligned}$$

The first three terms of Eq. (3) form the zero order of diffraction; the fourth and fifth terms produce two real images corresponding respectively to the horizontal and vertical Jones-vector components. The last two terms produce the virtual images.

A digital hologram is recorded by a black-and-white CCD camera (Basler A101f) and transmitted to a computer by a firewire port. The digital hologram $I_H(k, l)$ is an array of $N \times N = 512 \times 512$ 8-bit-encoded numbers resulting from the two-dimensional sampling of $I_H(x, y)$ by the CCD camera:

$$I_H(k, l) = \int_{k\Delta x - \Delta x/2}^{k\Delta x + \Delta x/2} \int_{l\Delta y - \Delta y/2}^{l\Delta y + \Delta y/2} I_H(x, y) dx dy, \tag{4}$$

where k, l are integers and $\Delta x, \Delta y$ define the sampling intervals in the hologram plane (pixel size) $\Delta x = \Delta y = L/N$ ($L \times L$ is the area of the sensitive chip).

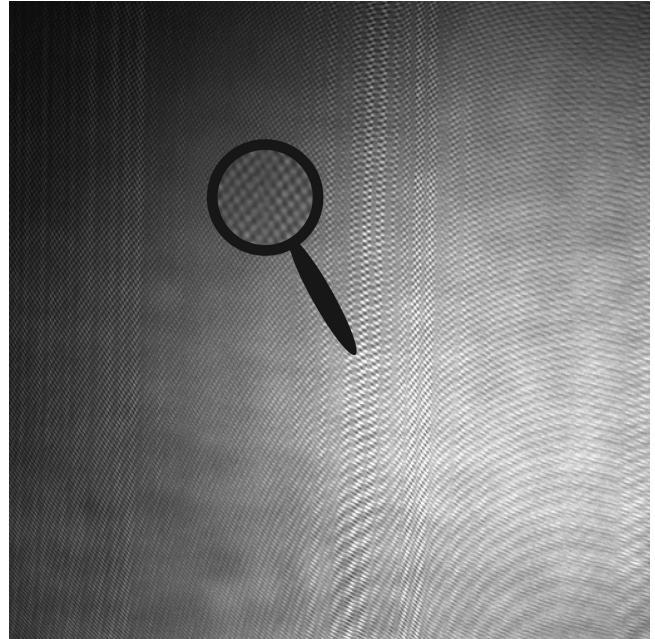


Fig. 2. Hologram of the nonstripped bent fiber. The magnifying glass permits one to visualize the two different curved fringe patterns corresponding to the interference of the object wave with the two orthogonally polarized reference waves.

Figure 2 presents a digital hologram recorded with the experimental setup presented in Fig. 1, with a 10 times magnification MO. The sample is a nonstripped bent optical fiber doped with 9 mol.% Germanium (made by Cabloptic SA, Switzerland) immersed in a refractive-index liquid of 1.4571 at 632 nm and room temperature (25 °C) matching the cladding refractive index (1.45704 at 632 nm) of the fiber.

We can see in Fig. 2 that the hologram appears as the superposition of two interference fringe patterns, one interference pattern for each reference wave. These fringes are curved because of the phase curvature produced by the MO and are not concentric with respect to the center of the image as a consequence of the off-axis geometry.

B. Spatial Filtering

By computing the Fourier transform (FT) of the hologram, we obtain its spectrum. Figure 3 presents the amplitude of this spectrum, where the frequencies of the zero-order of diffraction, of the real and virtual images, and of parasitic interferences can be seen. By applying two different spatial filterings on this spectrum, the spatial frequencies components corresponding to each virtual image are selected separately as explained in Ref. 14 (Fig. 4). Because the object wave has a range of propagation vectors and not a single propagation vector as described in Eq. (1), the frequencies for each virtual images are spread out and not concentrated in a point.

Computing the inverse FT of these filtered spectrums results in two filtered complex holograms, and the standard reconstruction algorithm can be applied on each filtered hologram as explained in the next

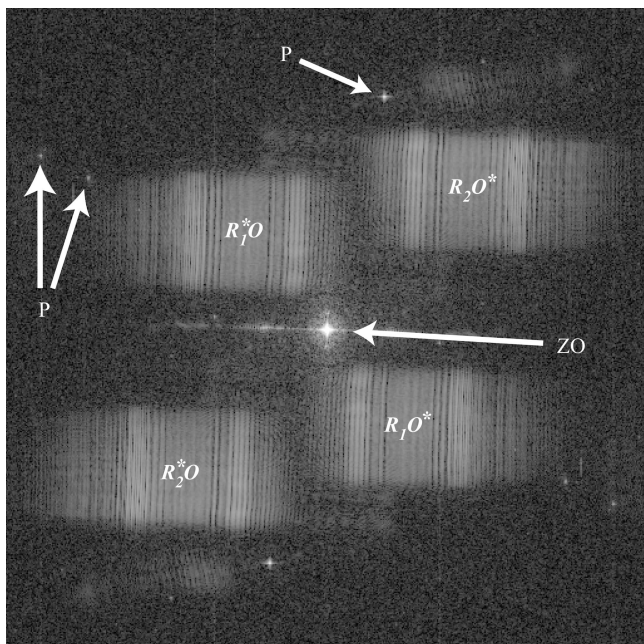


Fig. 3. Two-dimensional Fourier spectrum of the hologram presented in Fig. 2. ZO is the frequencies associated with the zero order of diffraction, and P indicates the contributions produced by parasitic interferences. $\mathbf{R}_1^* \mathbf{O}$ and $\mathbf{R}_1 \mathbf{O}^*$ are the frequencies associated with the horizontal polarization component corresponding, respectively, to the virtual and real images; $\mathbf{R}_2^* \mathbf{O}$ and $\mathbf{R}_2 \mathbf{O}^*$ are the frequencies associated with the vertical polarization component.

subsection. These two complex holograms are written

$$I_{Hj}(x, y) = \mathbf{R}_j^* \mathbf{O}, \quad (5)$$

for $j = 1, 2$.

C. Reconstruction Algorithm

In classical holography, illuminating the developed hologram successively with the two reference waves will perform the reconstruction. The reconstructed wavefronts are defined as follows:

$$\Psi_j = \mathbf{R}_j I_H. \quad (6)$$

In the Fresnel approximation the reconstructed wavefronts can be written as

$$\begin{aligned} \Psi_j(\xi, \eta) = & A \exp\left[\frac{i\pi}{\lambda d} (\xi^2 + \eta^2)\right] \\ & \times \int \int \mathbf{R}_j I_H(x, y) \exp\left[\frac{i\pi}{\lambda d} (x^2 \right. \\ & \left. + y^2)\right] \exp\left[\frac{i2\pi}{\lambda d} (x\xi + y\eta)\right] dx dy. \quad (7) \end{aligned}$$

As explained in Ref. 3, a discrete formulation of Eq. (7) involving a FT can be derived directly:

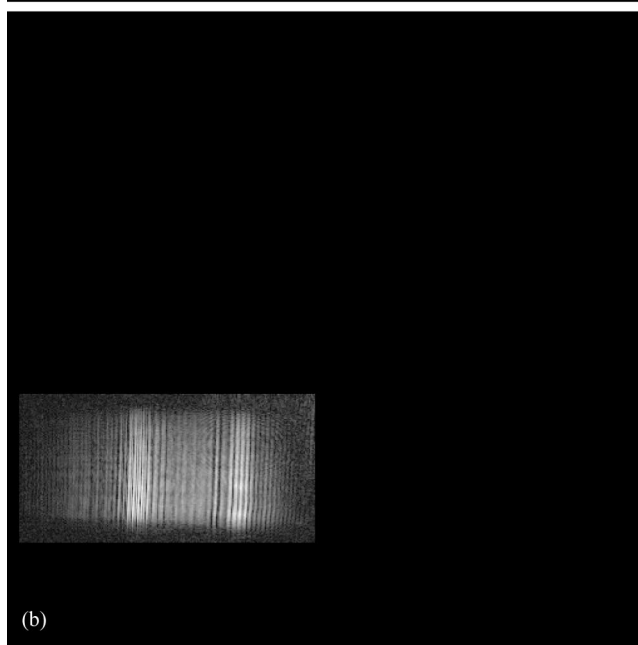
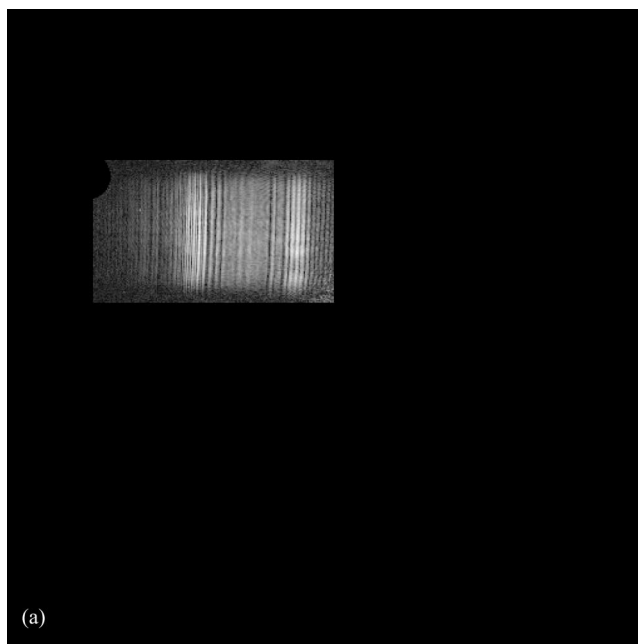


Fig. 4. Filtered two-dimensional Fourier spectra. Selection of the virtual image (a) for the horizontal polarization component, (b) for the vertical polarization component.

$$\begin{aligned} \Psi_j(m, n) = & A \exp\left[\frac{i\pi}{\lambda d} (m^2 \Delta \xi^2 + n^2 \Delta \eta^2)\right] \\ & \times \text{DFT} \left\{ \mathbf{R}_{Dj}(k, l) I_H(k, l) \exp\left[\frac{i\pi}{\lambda d} (k^2 \Delta x^2 \right. \right. \\ & \left. \left. + l^2 \Delta y^2)\right] \right\}_{m, n}, \quad (8) \end{aligned}$$

where m and n are integers ($-N/2 \leq m, n \leq N/2$), DFT is the discrete Fourier transform, and $A = \exp(i2\pi d/\lambda)/(i\lambda d)$, with d the reconstruction distance. $\Delta \xi$ and $\Delta \eta$ are the sampling intervals in the

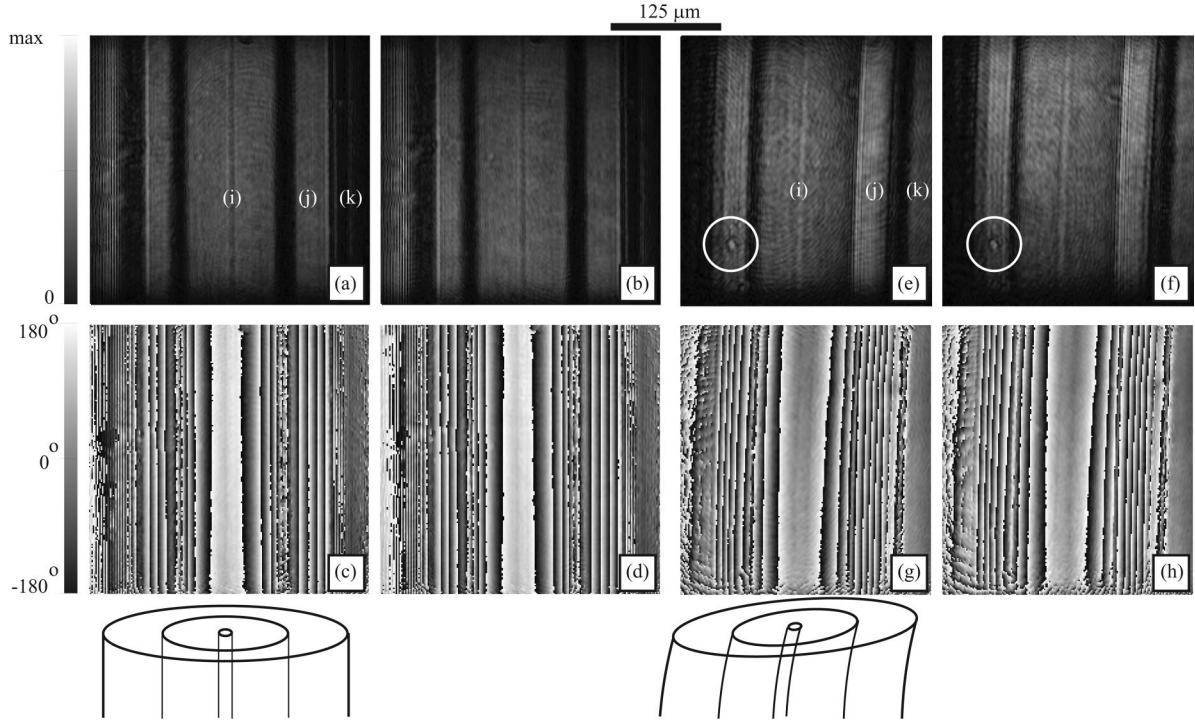


Fig. 5. Amplitude and phase reconstructions for an unbent fiber [(a)–(d)] and for a bent fiber [(e)–(h)]. (i) is the cladding region with focusing core in the middle, (j) is the coating region, and (k) is the refractive-index liquid region. (a), (e) $|o_1|$; (b), (f) $|o_2|$; (c), (g) phase (o_1); (d), (h) phase (o_2). Circles indicate positions of inhomogeneity in the azimuth due to some dust particles. The center of curvature is on the right of bent-fiber reconstructed images.

observation plane. \mathbf{R}_{Dj} are the digital reference waves defined as

$$\mathbf{R}_{Dj} = \exp[i(k_{Djx}k\Delta x + k_{Djy}l\Delta y)]. \quad (9)$$

The parameters k_{Djx} , k_{Djy} must be adjusted to match as closely as possible the propagation direction of the experimental reference waves \mathbf{R}_j .

In digital holographic microscopy, we have introduced³ a so-called digital phase mask $\Phi_j(m, n)$ in order to compensate the phase changes introduced by the microscope objective:

$$\Phi_j(m, n) = \exp\left[\frac{-i\pi}{\lambda} \left(\frac{m^2\Delta\xi^2}{p_{\xi_j}} + \frac{n^2\Delta\eta^2}{p_{\eta_j}} \right)\right], \quad (10)$$

where p_{ξ_j} and p_{η_j} are parameters that should be adjusted to compensate the wavefield curvature induced by introduction of the MO and to compensate also different eventual reference-wave curvatures. Hence the reconstructed wavefronts are

$$\begin{aligned} \Psi_j(m, n) = & A\Phi_j(m, n)\exp\left[\frac{i\pi}{\lambda d} (m^2\Delta\xi^2 + n^2\Delta\eta^2)\right] \\ & \times \text{DFT}\left\{ \mathbf{R}_{Dj}(k, l)I_H(k, l)\exp\left[\frac{i\pi}{\lambda d} (k^2\Delta x^2 \right. \right. \\ & \left. \left. + l^2\Delta y^2)\right] \right\}_{m, n}. \end{aligned} \quad (11)$$

Instead of reconstructing directly the recorded hologram I_H , the reconstructed wavefronts are computed using the filtered complex holograms I_{Hj} defined in Eq. (5):

$$\Psi_j = \mathbf{R}_{Dj}\mathbf{R}_j^*\mathbf{O}. \quad (12)$$

The off-axis geometry allows separating of the different diffraction orders, and therefore the different areas in the spectral content of the hologram corresponding to Ψ_1 and Ψ_2 . They can therefore be selected in the Fourier plane of the hologram. Using Eq. (1) in Eq. (12) and taking the amplitude contrasts [Figs. 5(a) and 5(b)] and the phase contrasts [Figs. 5(c) and 5(d)] of Ψ_1 and Ψ_2 yields gives

$$\begin{aligned} |\Psi_j| &= |r_j o_j| = |r_j| |o_j|; \quad \text{phase}(\Psi_j) \\ &= \text{phase}(o_j) - \text{phase}(r_j) + \phi_o. \end{aligned} \quad (13)$$

The adjustment of the half-wave plates orientation in the reference arms [$\lambda/2$ in Fig. 1(a)] achieves equal amplitudes for reference waves ($|r_1| = |r_2|$). Thus, the phase difference [$\Delta\phi_o = \text{phase}(o_2) - \text{phase}(o_1)$] and the azimuth [$\varepsilon = \text{atan}(|o_2|/|o_1|)$] parameters can be expressed from Eq. (13):

$$\tan(\varepsilon) = \frac{|\Psi_2|}{|\Psi_1|} = \frac{|o_2|}{|o_1|},$$

$$\Delta\phi_o = \text{phase}(\Psi_2) - \text{phase}(\Psi_1) + \Delta\phi_R, \quad (14)$$

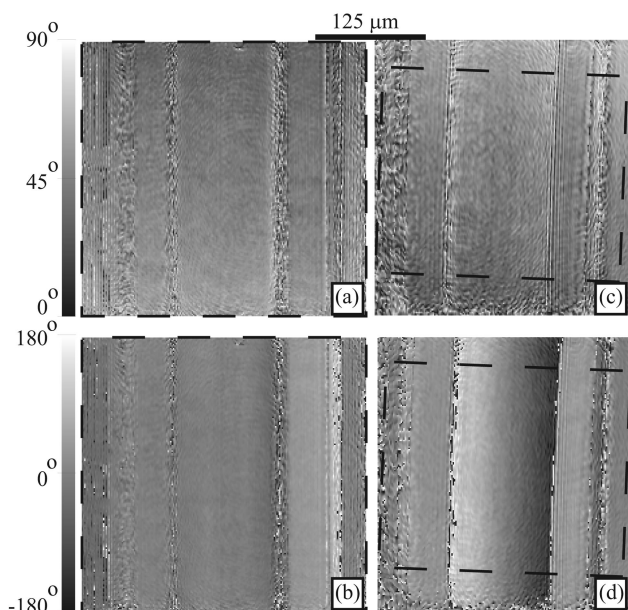


Fig. 6. SOP images reconstructed from images of Fig. 5: (a), (c) the azimuth and (b), (d) the phase difference for an unbent fiber (a), (b) and a bent fiber (c), (d). Mean profiles of Fig. 7 are defined along the major axis of dashed dark rectangles.

where $\Delta\varphi_R = \text{phase}(r_2) - \text{phase}(r_1)$ can be cancelled by a calibrated phase difference offset applied to the phase difference image.

The reconstructions of the SOP parameters (Fig. 6) are computed by adjusting the regions of interest (ROI) to superpose pixel by pixel the reconstructed images of Figs. 5(a)–5(d) and by computing then the Eq. (14) pixel by pixel.

3. Results and Discussion

A. Illustration of Method Principle: Stress in a Bent Optical Fiber

The goal of this subsection is to show that the PolDHM method permits one to image the polarization state of a microscopic object. A bent fiber is used because it is known that the stress induced by the bending creates birefringence (Ref. 15). The idea in this subsection is not to demonstrate the quantitative possibility of the method (discussed in Subsection 3.B) but to present the imaging capability. Indeed, to analyze quantitatively birefringence, it is better to strip off the coating of the fiber to study only the cladding. Here SOP parameters imaging of the entire fiber will be performed.

Figure 5 compares the amplitude and phase images for an unbent fiber [(a)–(d)] and a bent fiber [(e)–(h)]. The fiber core is visible in the amplitude images in the center of the cladding region [(i) in Fig. 5]. On the right, the coating region (j) and the refractive-index liquid region (k) are shown. The illuminating wave is transmitted through the entire fiber, and therefore the images presented in Figs. 5 and 6 are the integration of light properties over the depth of the fiber.

The borders between coating and cladding appear as dark lines on amplitude images and have an undefined phase. This phenomenon can be explained by the high refractive-index differences between each side of the borders; therefore the light passing near the borders undergoes a great deviation and is not collected by the MO so that no light coming from these areas reaches the CCD sensor.

There is an important difference of optical path length because there is also an important difference between the refractive indices of liquid and coating and between coating and cladding; therefore phase jumps appear in the phase images. On the other hand, a particle of dust floating in the liquid gives some contributions in amplitude [inside circles in Figs. 5(e) and 5(f)].

Figure 6 presents the SOP parameters of the unbent [(a) and (b)] and bent fiber [(c) and (d)]. It can be seen that the effect of dust particles disappears on the azimuth image [Fig. 6(c)]. The reason of this phenomenon is that this dust particle does not affect the polarization of the illuminating wave.

Figure 7 presents SOP values measured along the transverse section. A rectangular region of interest (ROI) with the major axis perpendicular to the fiber is selected on the SOP images (dashed rectangle in Fig. 6). The mean value along the small axis direction is taken for each point of the major axis. The azimuth and phase difference mean profile are plotted for the SOP images of the unbent and bent fibers.

The graph of Fig. 7(a) shows a uniform azimuth for the unbent fiber except in the border areas where azimuth is not well defined. For the bent fiber, the azimuth increases symmetrically from the center of the cladding region.

The graph of Fig. 7(b) shows first that without bending, the phase difference is not constant. Indeed, the phase-difference profile in the cladding region changes because of the fiber internal stress due to the fabrication process, and the right coating region has a phase difference of about 40° , due to the residual stress resulting from the winding of the fiber.

In the case of the bent fiber, the phase difference in the cladding region follows the theory.¹⁵ Indeed, the refractive index changes only in the direction perpendicular to the fiber axis (horizontal refractive index) and is constant in the direction parallel to the fiber axis (vertical refractive index). Furthermore, the horizontal refractive index increases for compressed areas and decreased for expanded area. Thus, because the phase difference is inversely proportional to the horizontal refractive index, it decreases in a compressed area and increases in an expanded area.

The bending of the fiber induces birefringence in the coating too. The comparison between the two curves indicates that the phase difference for the coating increases in the expanded area and decreases in the compressed area when the fiber is bent, as we can expect for the same reason explained above.

This example shows that the introduction of a microscope objective permits a 2D mapping of SOP parameters for microscopic objects. In the case of an

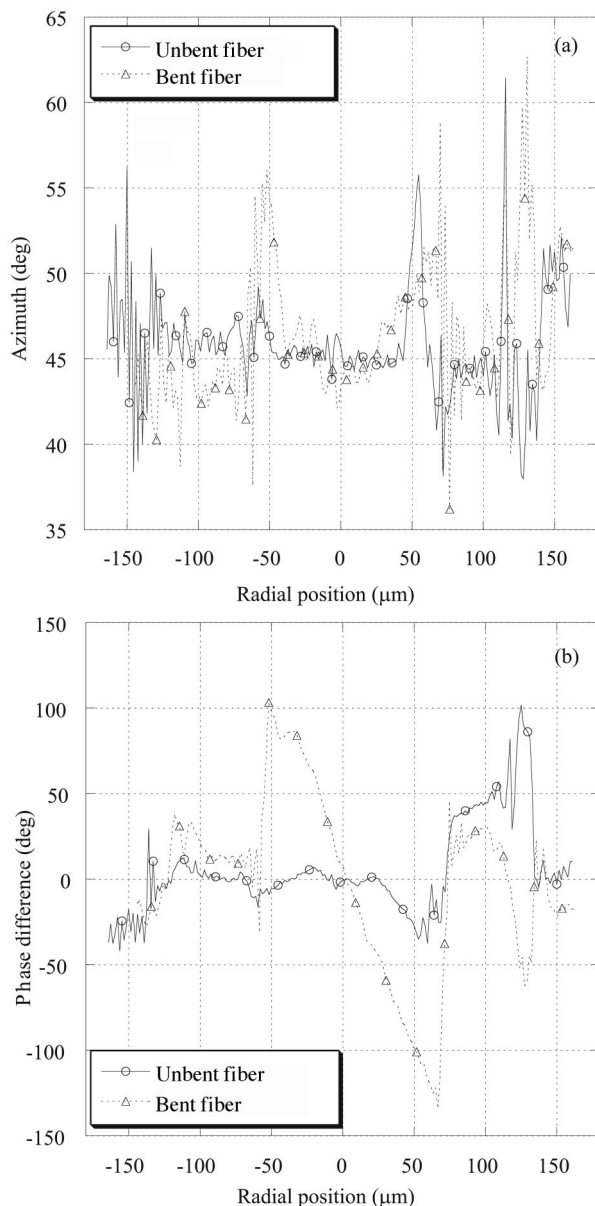


Fig. 7. Graphs of mean profiles defined by rectangle of Fig. 6: (a) the azimuth, (b) the phase difference.

optical fiber, the comparison between SOP images of an unbent fiber and a bent fiber reveals clearly a SOP modification due to the bending. The SOP images contrast is also due uniquely to the optical properties induced by the stresses. Therefore a map of the stresses in the optical fiber is obtained without suppressing the coating. It can be interesting for a quality control application, for instance.

B. Resolution and Efficiency Evaluation: Internal Stress in Optical Fiber

To evaluate the resolution of the phase-difference imaging, the same fiber with a suppressed coating and without bending is used as a sample. The goal is to image the birefringence due to the internal stress created during the fiber fabrication process.¹⁶ The

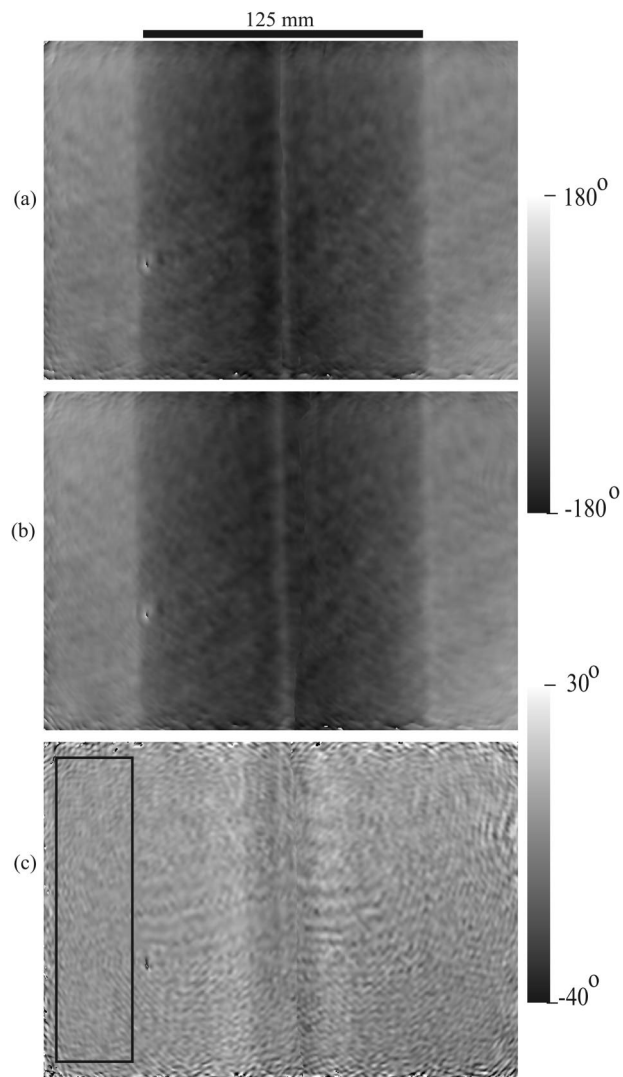


Fig. 8. Reconstructed phase and phase-difference images. (a) phase (o_1), (b) phase (o_2), (c) phase difference. The phase-difference standard deviation in the rectangle area is about 6 degrees.

fiber is immersed in the same refractive-index liquid as before. Figure 8 presents reconstructed images achieved with a 20 times magnification MO and a numerical aperture $N.A. = 0.5$: (a) phase (o_1), (b) phase (o_2), and (c) the phase difference. Because the refractive-index liquid is very close to the cladding refractive index, there are no phase jumps and the core is visible in the center of the fiber. The phase-difference images show clearly the birefringence due to internal stress. However, to evaluate the precision, a comparison with a reference method is necessary.

The setup used to obtain the reference birefringence profile is similar to the one presented in Ref. 17 and is a further development of a method already demonstrated in 1982.¹⁶ Light from a He-Ne laser is scattered by a rotating diffuser, collected by a lens, and linearly polarized at an angle θ . The polarized light passes successively through a quarter-wave plate and the optical fiber. The fiber axis is adjusted to an angle of 45° with respect to the optical axes of

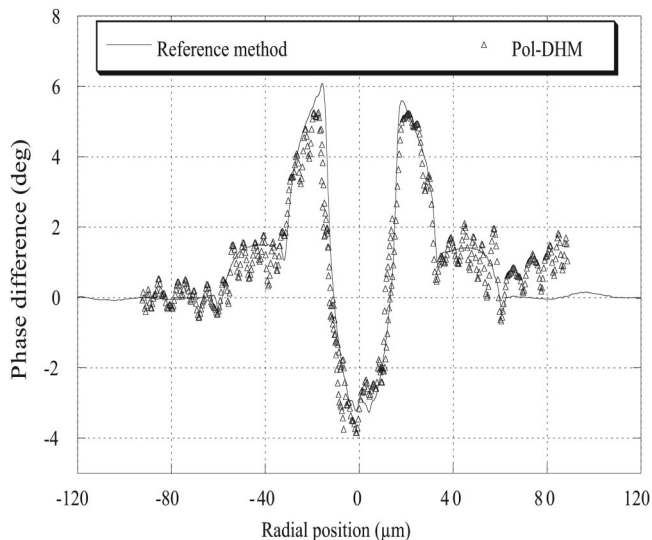


Fig. 9. Comparison between the phase-difference measurements performed with the reference method (solid curve) and performed with the Pol-DHM.

the quarter-wave plate. Thus, the light is again linearly polarized after having passed the fiber. The axis of polarization of the beam leaving the fiber is shifted by a certain angle $\Delta\theta$ with respect to the axis of the beam impinging on the quarter-wave plate. The angle shift $\Delta\theta$ is proportional to the birefringence introduced by the fiber. The shift in polarization angle is converted to an intensity modulation by an analyzer following the optical fiber. The resulting intensity distribution of the light behind the analyzer is

$$I(x, z) = I_{\max} \sin^2[\theta + \Delta\theta(x, z)]. \quad (15)$$

The intensity profile [Eq. (15)] is captured by a CCD camera for different angles θ of the light impinging on the quarter-wave plate. This allows the determination of the intensity minima with high accuracy, using a least-square fitting algorithm. At minimum intensity, $\theta = -\Delta\theta(x, z)$ in Eq. (15). Thus the spatial profile of the fiber-induced birefringence can be determined. The fiber is imaged on the CCD camera using a $20\times$ MO with a numerical aperture of 0.5, limiting the spatial resolution to about $0.8 \mu\text{m}$. The standard deviation in $\Delta\theta$ is better than 0.1° .

As to compare the Pol-DHM with the reference method, a phase-difference mean profile is taken from the Fig. 8(c) by computing the average phase difference on each column. Figure 9 presents the comparison between the phase difference measured with the reference method (solid curve) and with the Pol-DHM method (triangle).

In the reference method the intensity is measured over 36 different angles to determine the angle of minimum intensity. This leads to a phase-difference resolution of 0.1 degree. In contrary, to obtain a phase-difference profile by Pol-DHM, only one single acquisition is performed. In this case a one-dimensional phase-difference resolution of less than

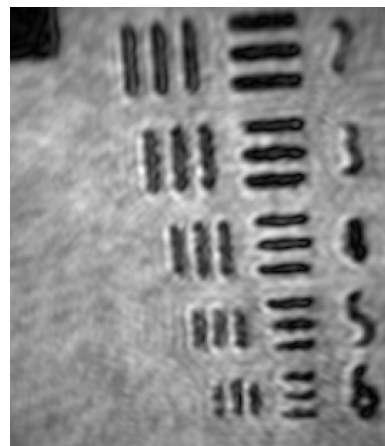


Fig. 10. $|o_1|$ image reconstruction of standard USAF target hologram recorded with a $20\times$ MO. The smallest elements correspond to 228 line pairs/mm.

2 degrees is obtained, which is comparable to standard methods.¹⁵ The two-dimensional phase-difference resolution is evaluated by adding the standard deviation measured out of the fiber area (rectangle in Fig. 8) with the one-dimensional resolution. The calculus gives a standard deviation about 6 degrees that gives a two-dimensional phase-difference resolution better than 8 degrees.

The spatial resolution of DHM is approximately equal to the diffraction limit of the MO as shown in Ref. 3. Therefore, the spatial resolution should be $0.61\lambda/\text{N.A.} \approx 0.8 \mu\text{m}$. However, because the MO was not used in its best performance in terms of spatial resolution for technical reasons, the effective spatial resolution is evaluated to about $2 \mu\text{m}$ by considering that the edges and middle of fiber core ($6.7 \mu\text{m}$) are well distinguishable. Figure 10 presents the $|o_1|$ reconstruction of a standard USAF target hologram recorded with the same setup. The smaller elements corresponding to 228 lines per millimeter are distinguishable, and therefore it confirms a spatial resolution of about $2 \mu\text{m}$.

4. Conclusion

In this paper, the existing techniques of polarization digital holography and digital holographic microscopy were joined together to achieve a new type of polarized-light microscope, the Pol-DHM. We have shown that this method permits, by the acquisition of a single hologram in off-axis geometry, to image the SOP parameters of the object wave transmitted through a microscopic sample with a spatial resolution about $2 \mu\text{m}$. Nonstripped bent and unbent fibers were used as microscopic samples to illustrate the principle of the method and its imaging capability. Finally, birefringence induced by internal stress in a stripped optical fiber was measured and compared with the results obtained with a reference method. The results of the two methods match quite well, and the Pol-DHM has a one-dimensional phase-difference resolution better than 2 degrees, that is comparable

to standard methods and a two-dimensional phase difference resolution better than 8 degrees. The next step of the Pol-DHM is to image the SOP of other birefringent objects, in transmission and reflection configuration, with biological samples in particular.

This work was funded through research grants 2153-067068.01 and 205320-103885/1 from the Swiss National Science Foundation.

References

1. V. D. Petrov, "Instantaneous holography with spraying of the developer," *J. Opt. Technol.* **69**, 92 (2002).
2. G. Pedrini, I. Alexeenko, W. Osten, and H. J. Tiziani, "Temporal phase unwrapping of digital hologram sequences," *Appl. Opt.* **42**, 5846–5854 (2003).
3. E. CuChe, P. Marquet, P. Dahlgren, C. Depeursinge, G. DelacrétaZ, and R. P. Salathé, "Simultaneous amplitude and quantitative phase-contrast microscopy by numerical reconstruction of Fresnel off-axis holograms," *Appl. Opt.* **38**, 6994–7001 (1999).
4. D. Gabor and W. P. Goss, "Interference microscope with total wavefront reconstruction," *J. Opt. Soc. Am.* **56**, 849–858 (1966).
5. P. Klysubun and G. Indebetouw, "A posteriori processing of spatiotemporal digital microholograms," *J. Opt. Soc. Am. A* **18**, 326–331 (2001).
6. F. Dubois, C. Minetti, O. Monnom, C. Yourassowsky, J.-C. Legros, and P. Kischel, "Pattern recognition with a digital holographic microscope working in partially coherent illumination," *Appl. Opt.* **41**, 4108–4119 (2002).
7. P. Ferraro, G. Coppola, S. De Nicola, A. Finizio, and G. Pierattini, "Digital holographic microscope with automatic focus tracking by detecting sample displacement in real time," *Opt. Lett.* **28**, 1257–1259 (2003).
8. A. W. Lohmann, "Reconstruction of vectorial wavefronts," *Appl. Opt.* **4**, 1667–1668 (1965).
9. T. Colomb, P. Dahlgren, D. Beghuin, E. CuChe, P. Marquet, and C. Depeursinge, "Polarization imaging by use of digital holography," *Appl. Opt.* **41**, 27–37 (2002).
10. T. Colomb, E. CuChe, F. Montfort, P. Marquet, and C. Depeursinge, "Jones vector imaging by use of digital holography: simulation and experimentation," *Opt. Commun.* **231**, 137–147 (2004).
11. R. Oldenbourg and G. Mei, "New polarized light microscope with precision universal compensator," *J. Microsc.* **180**, 140–147 (1995).
12. K. Oka and T. Kaneko, "Compact complete imaging polarimeter using birefringent wedge prisms," *Opt. Express* **11**, 1510–1519 (2003).
13. Y. Ohtsuka and K. Oka, "Contour mapping of the spatiotemporal state of polarization of light," *Appl. Opt.* **33**, 2633–2636 (1994).
14. E. CuChe, P. Marquet, and C. Depeursinge, "Spatial filtering for zero-order and twin-image elimination in digital off-axis holography," *Appl. Opt.* **39**, 4070–4075 (2000).
15. F. El-Diasty, "Interferometric determination of induced birefringence due to bending in single-mode optical fibers," *J. Opt. A: Pure Appl. Opt.* **1**, 197–200 (1999).
16. P. L. Chu and T. Whitbread, "Measurement of stresses in optical fiber and preform," *Appl. Opt.* **21**, 4241–4245 (1982).
17. Y. Park, T.-J. Ahn, Y. H. Kim, W.-T. Han, U.-C. Paek, and D. Y. Kim, "Measurement method for profiling the residual stress and the strain-optic coefficient of an optical fiber," *Appl. Opt.* **41**, 21–26 (1999).